Chinese Chemical Letters 34 (2023) 107538

Contents lists available at ScienceDirect

Chinese Chemical Letters

journal homepage: www.elsevier.com/locate/cclet

Temperature-controlled fabrication of hydrophilic manganese oxide microspheres as high-performance electrode materials for supercapacitors

Yuchen Wang[a], Yaoyu Liu[a], Ahsan Ejaz[b], Kai Yan[a,*]

[a] Guangdong Provincial Key Laboratory of Environmental Pollution Control and Remediation Technology, School of Environmental Science and Engineering, Sun Yat-sen University, Guangzhou 510275, China
[b] Department of Civil Engineering, Mirpur University of Science and Technology, AJK, Mirpur 10250, Pakistan

ARTICLE INFO

Article history:
Received 9 May 2022
Accepted 17 May 2022
Available online 20 May 2022

Keywords:
Temperature-controlled
Manganese oxide
Microsphere
Supercapacitors
Hydrophilic

ABSTRACT

The supercapacitive properties of manganese oxides (MnO_x) are strongly affected by their crystal structure. Nevertheless, the relationship between the crystal structure and supercapacitive performance of MnO_x is elusive. Herein, a temperature-controlled fabrication method was developed to achieve MnO_2, Mn_3O_4, MnO and Mn_2O_3 microspheres with various crystal structure as electrode materials tunable for supercapacitors. The detailed material and electrochemical characterizations revealed the structure-activity relationship of MnO_x microspheres by systematically investigating the effect of valence state, specific surface area, conductivity and morphology on supercapacitive performance. Among these MnO_x materials, nanoneedle-like MnO_2 delivered a relatively high specific capacitance of 274.1 F/g at 1 A/g due to a high Mn valence state of +4, a large specific surface area of 113.4 m^2/g and a desirable electronic conductivity of 1.73×10^{-5} S/cm. Furthermore, MnO_2 presented a remarkable cycle stability with 115% capacitance retention after 10,000 cycles owing to the enhancement of wettability. This work not only provides a facile strategy to modulate MnO_x crystal structure, but also offers a deep understanding of structure-dependent supercapacitive performance of MnO_x.

Nowadays, the growing energy crisis and environmental problem have accelerated the development of energy storage technologies [1,2]. Supercapacitors (SCs) are one of representative energy storage devices with the advantages of rapid charge/discharge rate, high specific power and long cycle life [3–6]. Manganese oxides (MnO_x) with multiple valence states have been considered as promising candidates of electrode materials for SCs due to their large theoretical specific capacitance value, natural abundance and environmental friendliness [7–9]. Generally, supercapacitive performance of MnO_x is characterized by their specific capacitance C_{MnO_x} and maximum power P_{max}, which are governed by the Mn valence and conductivity according to [10,11]: $C_{MnO_x} = Fn(Os_{max} - Os_{min})/\Delta V$ and $P_{max} = \Delta V^2/4R$, respectively, where F is Faraday constant, n is the mole number of Mn per unit mass, Os_{max} is the highest Mn oxidation state, Os_{min} is the lowest Mn oxidation state, ΔV is the potential range and R is the internal resistance of MnO_x. Except for Mn valence and conductivity, tunnel size also determines the supercapacitive performance of MnO_x by affecting the transportation and intercalation of electrolyte ions [12]. Since these aforementioned intrinsic material properties of MnO_x are highly dependent on their crystal structure [13,14], the modulation of MnO_x crystal structure is crucial to achieve ideal supercapacitive performance.

Numerous efforts have been carried out to investigate the effect of MnO_x crystal structure on their supercapacitive performance. For example, Devaraj and Munichandraiah [15] fabricated nanostructured α, β, γ, δ, λ-MnO_2 and compared their supercapacitive performance. Among these MnO_2 materials, the wide tunnel size and large surface area are key factors for α-MnO_2 to realize the outstanding maximum specific capacitance of 297 F/g. Hu *et al.* [16] derived Mn_3O_4 with different crystal structures/morphologies by adjusting the hydrothermal temperature and studied their electrochemical properties. Compared with other Mn_3O_4 materials, orthorhombic Mn_3O_4 nanofibers showed a relatively high specific capacitance of 235 F/g at 1 mV/s and excellent cycling performance of 80% capacitance retention after 10,000 cycles. To date, various crystal forms of MnO_x have been explored to some extent, the influence of MnO_x crystal structure on the supercapacitive per-

* Corresponding author.
E-mail address: yank9@mail.sysu.edu.cn (K. Yan).

https://doi.org/10.1016/j.cclet.2022.05.052
1001-8417/

formance remains elusive. Furthermore, although MnO_x have displayed high specific capacitance values, their limited capacitance retention (<90%) after long cycle times (>10,000 times) cannot meet the requirement of practical utilization [17]. Therefore, it is scientifically significant to optimize MnO_x crystal structure to achieve high specific capacitance and great cycling stability simultaneously.

Previously, our group have successfully synthesized MnO and Mn_2O_3 microspheres for efficient photo-Fenton removal of fluoroquinolone antibiotics through a facile hydrothermal method [18]. Inspired by this work, we reported a temperature-controlled methodology to obtain MnO_2, Mn_3O_4, MnO and Mn_2O_3 microspheres with different crystal structure. The structure-activity relationship of MnO_x microspheres was revealed by systematically investigating the effect of temperature on their valence state, specific surface area, conductivity and morphology, which are vital to their supercapacitive performance. Among these MnO_x materials, MnO_2 synthesized at lowest temperature realized the best supercapacitive performance with the following benefits: (1) The high valence state of MnO_2 microspheres determines high theoretical charge storage capacity of each Mn active site; (2) The microporous/mesoporous structure with high specific surface area could provide abundant active sites for energy storage; (3) The relatively stable Mn-O bonds suppress Jahn-Teller effect to achieve desirable electronic conductivity; (4) The enhanced wettability of MnO_2 microspheres during the cycling measurement results in an excellent cyclability. This work provides a deep insight of excellent electrochemical performance of temperature-dependent MnO_x which could be potentially expanded to other metal oxides in energy storage applications.

Fig. S1 (Supporting information) clearly shows the temperature-controlled synthesis route of MnO_x microspheres. First of all, MnO_2 microspheres were fabricated through a facile hydrothermal process at 90 °C. The formation process of MnO_2 was elucidated as $MnSO_4 + (NH_4)_2S_2O_8 + 2H_2O \rightarrow MnO_2 + (NH_4)_2SO_4 + 2H_2SO_4$ [19]. After that, as-prepared MnO_2 microspheres were calcined at 280, 500 and 600 °C under different atmospheres to obtain Mn_3O_4, MnO and Mn_2O_3 microspheres, respectively. Fabrication and characterization details of MnO_x are described in Supporting information.

X-ray diffraction (XRD) patterns are presented in Fig. S2 (Supporting information) to confirm the structure of as-prepared MnO_x materials. The characteristic peaks of MnO_2, Mn_3O_4, MnO and Mn_2O_3 matched well with standard PDF cards #44–0142, #24–0734, #07–0230 and #41–1442, respectively, implying the successful preparation of MnO_x materials. Based on the strongest peaks from MnO_2 (210), Mn_3O_4 (211), MnO (200) and Mn_2O_3 (222), the corresponding average particle size was estimated as 17.2, 12.7, 23.9 and 31.3 nm using the Scherrer equation [20]. As summarized in Fig. S3 (Supporting information), MnO_x materials synthesized at high temperature possessed large particle size. MnO_2 and Mn_3O_4 with the relatively small particle size and low crystallinity were expected to exhibit large surface area [21], which would be verified in the following porosity analysis.

The surface Mn valence and porosity information of MnO_x materials were analyzed by X-ray photoelectron spectroscopy (Fig. S4 in Supporting information) and N_2 adsorption-desorption isotherms (Fig. S5 in Supporting information), respectively. As shown in Fig. S4a, survey spectra indicated the existence of Mn and O elements in MnO_x materials except the reference C peak. According to high resolution Mn 2p spectra (Fig. S4b), two distinct peaks of MnO_2 at 654.1 eV and 642.1 eV were assigned to Mn $2p_{1/2}$ and Mn $2p_{3/2}$, respectively, which are consistent with the reported values [22]. By decreasing valence state of Mn, the peaks of Mn $2p_{1/2}$ and Mn $2p_{3/2}$ gradually shifted to low binding energy. For MnO, the Mn $2p_{1/2}$ peak at 653.5 eV and Mn $2p_{3/2}$ peak at 641.4 eV revealed that the valence state of Mn was +2 [23]. Fig. S5a displays N_2 adsorption-desorption isotherms of MnO_x materials. The isotherms with the combination of type I and type IV features demonstrated the presence of micropores and mesopores [24], which were confirmed by the pore size distribution (Fig. S5b). The pore size distribution of MnO_x materials was mainly centered at around 1.0 and 3.6 nm. Consequently, the Brunauer-Emmett-Teller (BET) specific surface area of MnO_2, Mn_3O_4, MnO and Mn_2O_3 were calculated as 113.4, 83.5, 57.4 and 76.9 m^2/g, respectively. The relatively high specific surface area of MnO_2 and Mn_3O_4 were in good agreement with XRD results. As summarized in Table S1 (Supporting information), MnO_2 possessed the largest BET specific surface area and total pore volume, which provide plenty of actives sites for energy storage.

Electronic conductivity of MnO_x materials were investigated by four-point probe measurements. As displayed in Fig. 1a, the electronic conductivity values of MnO_2, Mn_3O_4, MnO and Mn_2O_3 were calibrated as 1.73×10^{-5}, 4.15×10^{-7}, 1.79×10^{-7} and 5.89×10^{-7} S/cm, respectively. It is reported that the electronic conductivity of MnO_x materials was affected by Jahn-Teller effect [25], which was also determined by the Mn-O bond length in MnO_6 octahedra [26]. According to the comparison of average Mn-O bonding distance between MnO_x materials (Fig. 1b), MnO_2 possessed the shortest average Mn-O bond length, indicating that the disruptive Jahn-Teller distortion is effectively suppressed in the crystal structure of MnO_2 [26]. Therefore, MnO_2 with high structural stability achieved desirable electronic conductivity, which is beneficial for electron transfer in energy storage processes.

Transmission electron microscopy (TEM) was used to study morphologies and microstructure of MnO_x materials. All MnO_x materials showed spherical morphologies with an average diameter of approximately 2 μm (Figs. 2a, d, g and j), indicating that the calcination temperature has negligible effects on the size of porous MnO_x microspheres. The magnified TEM image in Figs. 2b illustrated that MnO_2 microspheres were assembled by slender nanoneedles. The high-resolution transmission electron microscopy (HR-TEM) image (Fig. 2c) on these nanoneedles clearly displayed well-defined lattice fringes with *d*-spacing of 0.24 nm, which is attributed to the crystal plane of (210) from MnO_2. By increasing calcination temperature, orthorhombic MnO_2 were phase-transformed to tetragonal Mn_3O_4, cubic MnO and cubic Mn_2O_3. Accordingly, the assembly unit of MnO_x microspheres was changed from nanoneedles to nanowires (Fig. 2e), nanorods (Fig. 2h) and large-size irregular nanorods (Fig. 2k). Furthermore, distinct lattice fringes on these assembly units were observed from HR-TEM images (Figs. 2f, i and l) to further confirm the formation of Mn_3O_4, MnO and Mn_2O_3, respectively.

The supercapacitive performance of MnO_x electrodes were investigated by cyclic voltammetry (CV), galvanostatic charge/discharge (GCD), electrochemical impedance spectroscopy (EIS) and cycling measurements. In Fig. 3a, CV curves of MnO_x electrodes displayed distinct redox peaks, which originate from the reaction between MnO_x and OH^- in alkaline electrolyte [27]:

$$Mn^{3+}_{0.55}Mn^{4+}_{1.45}O_4 + 0.45OH^- \leftrightarrow Mn^{4+}_2O_{4.225} + 0.225H_2O + 0.55e^-$$

and $Mn^{4+}_2O_{4.225} + 6OH^- \leftrightarrow Mn^{7+}_2O_{7.225} + 3H_2O + 6e^-$.

With the increase of Mn valence state, the positions of anodic peaks shifted to relatively high potential. Compared to other MnO_x electrodes, the CV curve of the MnO_2 electrode explicitly showed two pairs of redox peaks with highest specific current values, indicating the greatest charge storage ability. Afterwards, CV curves of MnO_2 electrode from 5 mV/s to 50 mV/s (Fig. 3b) showed an unchangeable shape with negligible ohmic polarization, demonstrating an excellent electrochemical reversibility. Subsequently, the

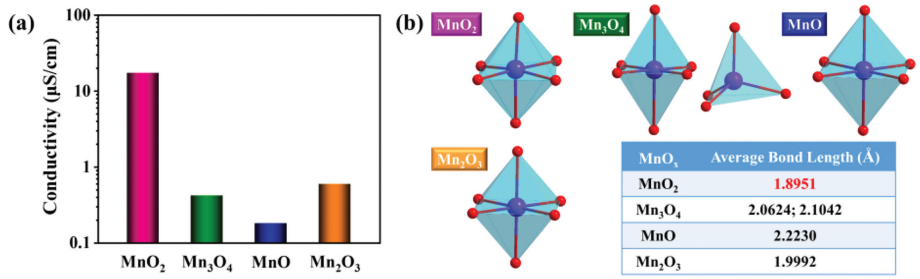

Fig. 1. (a) Conductivity values of MnO_x materials. (b) The comparison of average Mn-O bonding distances between MnO_x materials.

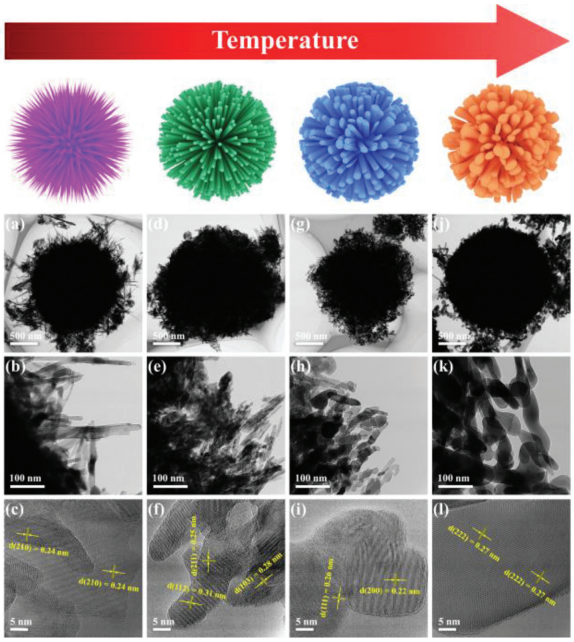

Fig. 2. TEM images of (a, b) MnO_2, (d, e) Mn_3O_4, (g, h) MnO and (j, k) Mn_2O_3. HR-TEM images of (c) MnO_2, (f) Mn_3O_4, (i) MnO and (l) Mn_2O_3.

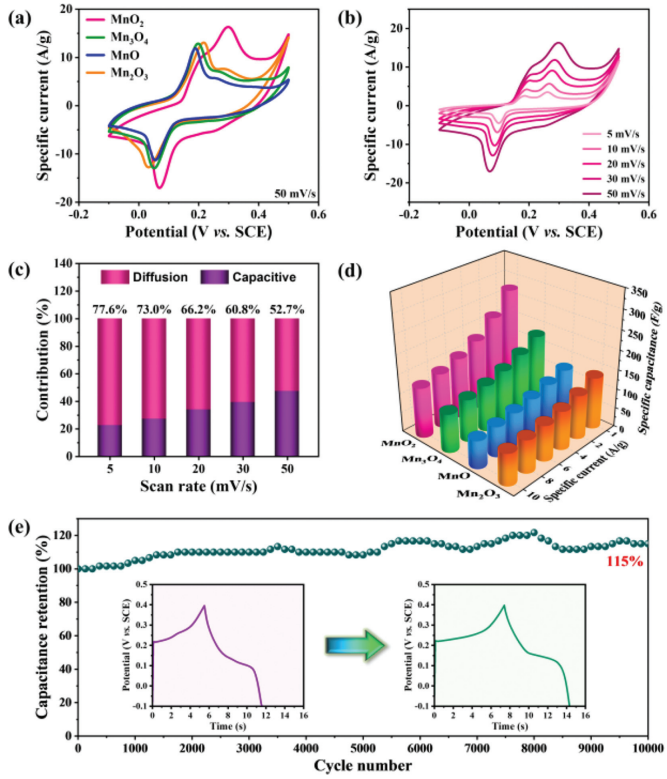

Fig. 3. (a) CV curves of MnO_x electrodes at 50 mV/s. (b) CV curves of MnO_2 electrode at scan rates of 5, 10, 20, 30 and 50 mV/s. (c) Contribution ratio of capacitive and diffusion-controlled mechanism at different scan rates for the MnO_2 electrode. (d) Specific capacitance values of MnO_x electrodes at different specific currents. (e) Cycle stability of MnO_2 electrode at 10 A/g (inset: GCD curves before and after cycling test).

electrochemical kinetics of MnO_x electrodes were studied according to the power-law relationship between the cathodic peak current (i) and the scan rate (ν): $i = a\nu^b$ [28]. The b-value of 0.5 and 1.0 correspond to the Faradaic diffusion-controlled and capacitive mechanism, respectively. By fitting in Fig. S6 (Supporting information), the b-value were derived as approximately 0.6, denoting that the charge storage mechanism of MnO_x electrodes are mainly controlled by diffusion-controlled process. Specifically, the contribution of diffusion-controlled and capacitive mechanism were separated by applying the formula: $i = k_1\nu + k_2\nu^{0.5}$ [28]. For the MnO_2 electrode (Fig. 3c), the diffusion-controlled contribution was calculated as 77.6% at 5 mV/s, which is in accordance with the b-value analysis. With the increasing scan rate, the diffusion-controlled contribution decreased to 52.7% at 50 mV/s due to the inherent nature of battery-like redox reactions [29].

Fig. S7 (Supporting information) presents GCD curves of MnO_x electrodes at 2 A/g. The nonlinear shape of these GCD curves represented the faradaic processes in MnO_x electrodes, which are in good agreement with above CV curves. On the basis of GCD curves at various specific currents (Fig. S8 in Supporting information), the specific capacitance values of MnO_x electrodes were summarized in Fig. 3d. Among these MnO_x electrodes, the MnO_2 electrode realized the highest specific capacitance of 274.1 F/g, which is comparable or superior to relevant reported publications (Table S2 in Supporting information). Furthermore, the comparison of Nyquist plots of MnO_x electrodes in Fig. S9 (Supporting information) was consistent with previous electrochemical analyses. After fitting the impedance data with an equivalent circuit (Table S3 in Supporting information), the MnO_2 electrode exhibited the relatively low equivalent series resistance R_{ESR} (0.36 Ω) and charge transfer resistance R_{ct} (8.29 Ω), which correspond to high electronic conductivity and rapid electrolyte diffusion into the micro/mesopores of MnO_2 microspheres [30].

Based on above mentioned material and electrochemical characterizations, the enhanced supercapacitive performance of MnO_2 electrode can be attributed to following reasons: (1) The high Mn valence state of MnO_2 microspheres enabled more hydroxide ions to interact with each Mn active site; (2) MnO_2 microspheres with the high specific surface area (113.4 m^2/g) and unique microporous/mesoporous structure provided abundant Mn active sites; (3) MnO_2 with minimized Jahn-Teller distortion realized high elec-

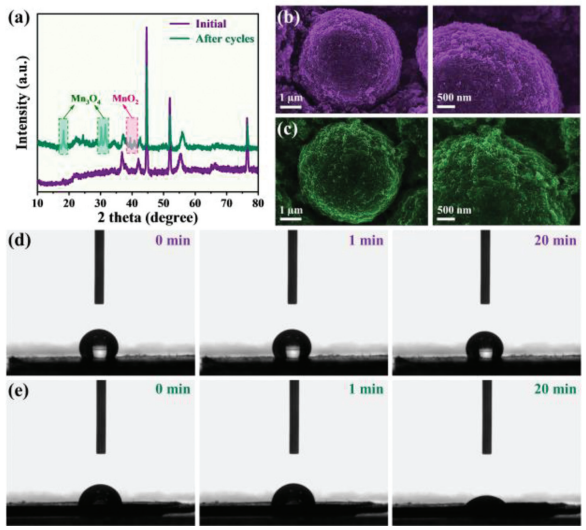

Fig. 4. (a) XRD patterns of MnO_2 electrode before and after cycling test. SEM images of MnO_2 electrode (b) before and (c) after cycling test. Contact angle measurements with 6 mol/L KOH electrolyte of MnO_2 electrode (d) before and (e) after cycling test at 0, 1 and 20 min.

tronic conductivity (1.73×10^{-5} S/cm), which is conducive to the fast electron transport for electrochemical kinetics.

The cycling performance of MnO_2 electrode at 10 A/g is illustrated in Fig. 3e. It is interesting that the capacitance retention of MnO_2 electrode increased to 115% after 10,000 cycles. Electrochemical characterizations after cycling test were carried out to elucidate the unpredictable enhancement. Fig. S10 (Supporting information) displays CV curves of MnO_2 electrode at initial and after cycle states. Compared to the initial state, the CV curve of cycled MnO_2 electrode showed a pair of redox peaks with greater specific current at higher potential, illuminating that the charge storage processes became more preferential to proceed between relatively higher valence states of Mn. Meanwhile, GCD curves with higher charge/discharge platform in Fig. S11 (Supporting information) presented the same tendency. Furthermore, according to the *b*-value calculation from Figs. S12 and S13a (Supporting information), the charge storage mechanism changes from diffusion-controlled process to diffusion/capacitive-controlled processes during the cycling measurement. Concretely, as depicted in Fig. S13b (Supporting information), the capacitive contribution of MnO_2 electrode was increased by 14.0%, 15.2%, 16.8%, 17.1% and 16.6% after 10,000 cycles at scan rates of 5, 10, 20, 30 and 50 mV/s, respectively. In other words, fast Faradaic redox reactions were proceeded at MnO_2 electrode after long-term GCD measurements. Consequently, the cycled MnO_2 electrode possessed much higher rate capability (75.2%) than the initial MnO_2 electrode (47.4%) and retained the maximum specific capacitance, which were derived from Fig. S14 (Supporting information).

Structural and morphological characterizations including XRD, SEM and contact angle measurements were performed to explain the enhanced rate capability of MnO_2 electrode after cycling test. From XRD results in Fig. 4a, the appearance of characteristic peaks of Mn_3O_4 indicated the phase transformation from MnO_2 to MnO_2/Mn_3O_4 during the cycling test. Meanwhile, new characteristic peaks at around 40° were observed and attributed to MnO_2 (111) and (002), revealing the exposure of more Mn active sites. Although the specific capacitance of Mn_3O_4 was lower than that of MnO_2 at 1 A/g, the competing effect of phase transformation and increased active sites led to the invariant maximum specific capacitance of MnO_2 electrode. Figs. 4b and c show SEM images of MnO_2 electrode at initial and after cycle states. After cycling test, the spherical morphology of MnO_2 materials was almost unchanged without any agglomeration. Afterwards, the wettability of initial and cycled MnO_2 electrode was distinctly distinguished in Figs. 4d and e, respectively. In the 20 min measurement period, the contact angle of initial MnO_2 electrode was kept constant at 120° whereas the contact angle of cycled MnO_2 electrode decreased from 80° to 40°. According to Young's equation, the MnO_2 electrode was changed from hydrophobicity to hydrophilicity with the electrolyte in cycling process. The enhanced wettability improves the interaction between electrolyte ions and Mn active sites, which enhances utilization of active sites of MnO_2 electrode [31,32]. Moreover, another contrast experiment was designed to further verify the high wettability of cycled MnO_2 electrode. After soaking the cycled MnO_2 electrode in the electrolyte for 1 day, MnO_2 spheres covered with shells were observed in Fig. S15 (Supporting information). Compared to EDS elemental mappings of initial MnO_2 electrode (Figs. S16 and S17 in Supporting information), the shell was mainly composed of potassium ions, revealing that MnO_2 spheres in the cycled electrode are more hydrophilic to the electrolyte. Therefore, the enhanced specific capacitance of MnO_2 electrode during cycling test is mainly attributed to the intimate relationship between the electrode material and electrolyte.

In conclusion, we have successfully fabricated MnO_2, Mn_3O_4, MnO and Mn_2O_3 microspheres through a facile temperature-controlled method. Compared with other MnO_x microspheres, MnO_2 realized a higher Mn valence state of +4, a larger specific surface area of 113.4 m^2/g and a greater electronic conductivity of 1.73×10^{-5} S/cm, which are beneficial for enhancing the supercapacitive performance. Accordingly, MnO_2 possessed a relatively high specific capacitance of 274.1 F/g at 1 A/g and showed a remarkable capacitance retention of 115% after 10,000 cycles. This work provides an important guidance for understanding and optimizing the supercapacitive performance of temperature-dependent MnO_x.

Declaration of competing interest

The authors declare that they have no known competing financial interests or personal relationships that could have appeared to influence the work reported in this paper.

Acknowledgments

This work was supported by Key-Area Research and Development Program of Guangdong Province (No. 2019B110209003), Guangdong Basic and Applied Basic Research Foundation (No. 2019B1515120058), the Scientific and Technological Planning Project of Guangzhou, China (No. 202206010145), National Natural Science Foundation of China (No. 22078374), National Key R&D Program of China (No. 2020YFC1807600), National Ten Thousand Talent Plan and Hundred Talent Plan (No. 201602) from Sun Yat-sen University.

Supplementary materials

Supplementary material associated with this article can be found, in the online version, at doi:10.1016/j.cclet.2022.05.052.

References

[1] L. Lin, J. Chen, D. Liu, et al., Adv. Energy Mater. 10 (2020) 2002621.
[2] V. Dusastre, L. Martiradonna, Nat. Mater. 16 (2017) 15.
[3] J. Feng, X. Zhang, Y. Xu, et al., Energy Storage Mater. 46 (2022) 278–288.
[4] C. Liu, Q. Li, K. Wang, Renew. Sustain. Energy Rev. 150 (2021) 111408.
[5] Y. Zhou, H. Qi, J. Yang, et al., Energy Environ. Sci. 14 (2021) 1854–1896.
[6] K. Li, X. Liu, T. Zheng, et al., Chem. Eng. J. 370 (2019) 136–147.
[7] A. Zhang, R. Gao, L. Hu, et al., Chem. Eng. J. 417 (2021) 129186.
[8] L. Shi, Y. Wang, P. Zou, et al., Chin. Chem. Lett. 29 (2018) 592–595.

[9] J. Kang, A. Hirata, L. Kang, et al., Angew. Chem. Int. Ed. 52 (2013) 1664–1667.
[10] P. Guillemet, T. Brousse, O. Crosnier, et al., Electrochim. Acta 67 (2012) 41–49.
[11] Y. Wu, C. Cao, Sci. China Mater. 61 (2018) 1517–1526.
[12] Y. Hu, Y. Wu, J. Wang, Adv. Mater. 30 (2018) 1802569.
[13] Y. Liu, X. Wu, Chin. Chem. Lett. 33 (2022) 1236–1244.
[14] L. Wei, Z. Wang, Y. Liu, et al., J. Hazard. Mater. 416 (2021) 126117.
[15] S. Devaraj, N. Munichandraiah, J. Phys. Chem. C 112 (2008) 4406–4417.
[16] Y. Hu, Y. Zhang, D. Yuan, et al., Nanoscale Horiz. 2 (2017) 326–332.
[17] A. Zhang, R. Zhao, L. Hu, et al., Adv. Energy Mater. 11 (2021) 2101412.
[18] A. Wang, H. Wang, H. Deng, et al., Appl. Catal. B: Environ. 248 (2019) 298–308.
[19] N. Li, X. Zhu, C. Zhang, et al., J. Alloy. Compd. 692 (2017) 26–33.
[20] D. Gangwar, C. Rath, Phys. Chem. Chem. Phys. 22 (2020) 14236–14245.
[21] T. Falk, S. Anke, H. Hajiyani, et al., Catal. Sci. Technol. 11 (2021) 7552–7562.
[22] L. Mo, H. Zheng, J. Alloy. Compd. 788 (2019) 1162–1168.
[23] Z. Cui, Q. Liu, C. Xu, et al., J. Mater. Chem. A 5 (2017) 21699–21708.
[24] S. Liu, Y. Liang, W. Zhou, et al., J. Mater. Chem. A 6 (2018) 12046–12055.
[25] L. Liu, Y. Luo, W. Tan, et al., J. Colloid Interface Sci. 482 (2016) 183–192.
[26] J.U. Choi, J. Kim, J.Y. Hwang, et al., Nano Energy 61 (2019) 284–294.
[27] Q. Zhang, M.D. Levi, Q. Dou, et al., Adv. Energy Mater. 9 (2019) 1802707.
[28] Y. Mao, Y. Chen, J. Qin, et al., Nano Energy 58 (2019) 192–201.
[29] S.M. Ingole, S.T. Navale, Y.H. Navale, et al., J. Solid State Electrochem. 21 (2017) 1817–1826.
[30] G. Zhang, L. Ren, Z. Yan, et al., Chem. Commun. 53 (2017) 2950–2953.
[31] Y. Wang, Y. Liu, Z. Chen, et al., Green Chem. Eng. 3 (2022) 55–63.
[32] Y. Zhang, M. Park, H.Y. Kim, S.J. Park, J. Colloid Interface. Sci. 500 (2017) 155–163.